Dynamic Response of Pile-Slab Retaining Wall Structure under Rockfall Impact

Peng Zou[1, 2, 3], Gang Luo[1, *], Yuzhang Bi[4], Hanhua Xu[2, 3]

1. *Faculty of Geosciences and Engineering, Southwest Jiaotong University, Chengdu 611756, China*

2. *Kunming Prospecting Design Institute of China Nonferrous Metals Industry Co., Ltd, Yunnan 650051, Chin*a

3. *Yunnan Key Laboratory of Geotechnical Engineering and Geohazards, Kunming, 650051, China*

4. *College of Resources and Environment, Fujian Agriculture and Forestry University, Fuzhou 350002, China*

***Corresponding author at:** Faculty of Geosciences and Engineering, Southwest Jiaotong University, Chengdu 611756, China

E-mail addresses: luogang@home.swjtu.edu.cn (G. Luo).

Abstract: The pile-slab retaining wall has gained widespread utilization in rockfall mitigation engineering, attributed to its excellent impact resistance, substantial interception height, and reliable structural durability. The numerical experiments investigate the dynamic response of a pile-slab retaining wall under the various impact conditions of rockfall. Results reveal that: (1) during the impact process, the stress, strain, and concrete damage of the structure gradually spread from the impact center to entire structure and ultimately result in permanent deformation; (2) the lateral displacement of the pile at the ground surface and the concrete damage under the pile as the impact center is greater than those under the slab as the impact center, implying that the impact location has a significant influence on the stability of the structure; (3) there is a positive correlation between the response indexes (impact force, interaction force, lateral deformation of pile and slab, concrete damage, and the impact velocities; (4) within the discussed impact scenarios, the rockfall peak impact force, the ratio of peak impact force to peak interaction force, and lateral displacement of pile at the ground surface had strong linear relationships with rockfall energy. Utilizing this relationship, the estimated maximum impact energy that the pile-slab retaining wall can withstand is 905 kJ in this study when the structure top is taken as the impact point.

Keywords: rockfall, pile-slab retaining wall, numerical simulation, dynamic response

List of symbols

P	Actual lateral soil resistance (kPa).	F_{dm}	Peak impact force (kN).
P_{u}	Ultimate lateral soil resistance (kPa).	F_{im}	Peak interaction force (kN).
$S_{\mathrm{u\_cu}}$	Consolidated isotropic undrained tri-axial shear strength of soil (kPa/m).	α	Ratio of the peak impact force to the peak interaction force (%).
y	Actual lateral soil deformation (m).	S_{mpt}	Maximum the lateral displacement of pile at the ground surface (mm).
B	Pile width (m).	N_d	Number of damage failure units.
z	Depth below the ground surface (m).	β	Ratio of damage failure units to overall structure units (%).
S_{p}	Shape correction factor of pile section.	m	Impactor mass (kg).
E	Initial kinetic energy of impactor.	v	Initial velocity of impactor (m/s).

1. Introduction

Rockfall disaster are a great threat to roads, railways, buildings and inhabitants in mountainous terrain (Hungr et al., 2014; Crosta and Agliardi, 2004; Shen et al., 2019). It can be described as a process that the rapid bouncing, rolling and sliding movement of one (or several) boulders down a slope (Peila and Ronco, 2009). Muraishi et al. (2005) surveyed 607 rockfall events found that about 68% of rockfall events have an impact energy of less than 100 kJ, whereas 90% have less than 1000 kJ. Chau et al. (2002) indicated that the rotational kinetic energy of rockfall only accounts for 10% of the total kinetic energy. To mitigate such geological hazards, scholars and engineers have proposed different types of technical solutions. Two primary categories of defensive measures are commonly employed: active and passive. Active protection measures mainly include: masonry protection, reinforcement protection (grouting, anchor rod, and anchor cable), initiative protective net, etc (Yang et al., 2019). Passive protection measures include: passive flexible protection (Yu et al., 2021), rockfall shed gallery (Zhao et al., 2018), rockfall retaining wall, etc. Considering many factors such as technology and economy, rockfall retaining wall is often used in practical engineerin (Volkwein et al., 2011).

Currently, various types of retaining walls are utilized in engineering projects aimed at intercepting rockfall. These include masonry retaining walls, reinforced concrete (RC) retaining walls, reinforced soil retaining walls, and pile-slab retaining walls (PSRW). Due to inherent structural weakness of these walls, their ability to absorb the impact energy from rockfall is limited (Mavrouli et al., 2017). To enhance the impact resistance, the reinforced concrete retaining walls have been utilized (Yong et al., 2020). These structures can intercept rockfall impact energy ranging approximately from 120 to 500 kJ (Maegawa et al., 2011). To prevent concrete from being damaged by the direct impact of rockfall, a buffer layer is generally added in front of the structure for protection, such as reinforced soil and gabion cushion (Perera et al., 2021). Although the impact resistance of the structure has been improved, there is still a problem of limited interception height. When the required interception height is large, the foundation size has to be increased to prevent the structures from overturning. In order to mitigate against rockfall events involving higher energy levels, numerous researchers have proposed the implementation of reinforced soil retaining walls. Extensive studies have been conducted in this regard, demonstrating that the structures can effectively intercept rockfall impact energies exceeding 5000 kJ (Lambert et al., 2009). Moreover, geosynthetic have proven to be efficacious in reducing wall stresses (Lu et al., 2021). However, the structure requires a substantial spatial footprint and poses an overturning risk during construction in steep terrain (Peila et al., 2007). Additionally, when the topography at the wall site features steep slopes, the available space behind the wall for accommodating rockfalls is limited.

In response to the challenges posed by steep terrains, narrow site conditions, and suboptimal foundation conditions in mountainous terrain, Hu et al. (2019) introduced the PSRW structure. The structures are composed of a buffer layer and an anti-slip pile-slab structure. It has found widespread application in southwestern China (Fig. 1). Due to its implementation of pile foundations, this structure possesses characteristics such as a small footprint, high interception height, and ease of construction. However, the current PSRW design verification is to treat the structure as an underground continuous wall (CAGHP, 2019). And, due to the composite nature of this structure, the dynamical response at various impact points remains ambiguous. The maximum impact energy that the structure can withstand has also not been thoroughly investigated. It can lead to potential underestimation of failure possibilities (Fig. 1d). At the same time, the existing research focuses on the single slab and pile impacted by rockfall (Wu et al., 2021; Yong et al., 2021).

Fig. 1. PSRW in south-western China (a) Kongyu town (b) Jiuzhaigou nature reserve (c) Zhenjiangguan tunnel exit in Chengdu-lanzhou railway (d) Wenchuan-Maerkang expressway.

Therefore, analysis of structural dynamic response and concrete damage is crucial to determine its effectiveness in mitigating rockfall hazards. Based on the unique advantages of the finite element method, this study employs the LS-DYNA to simulate the complete process of rockfall impacting on PSRW. This methodology has been widely adopted by numerous researchers and demonstrated as suitable for simulating impact problems of reinforced concrete structure (Zhong et al., 2022; Fan et al., 2022; Bi et al., 2023). In conclusion, a full-scale numerical model of a four-span pile-slab retaining wall satisfying specification requirements is established. The rationality of the selected material constitutive models and a numerical algorithm was validated by reproducing two physical model tests. The structure's dynamic behavior under different impact velocities and impact centers is discussed（Fig. 2). The results provide insights into sturcture dynamic response analysis of the PSRW and serve as a benchmark for further research.

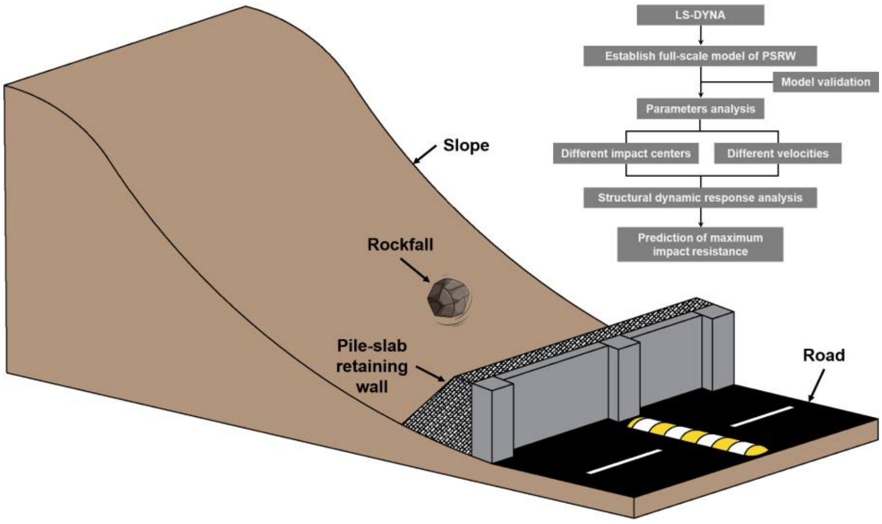

Fig. 2 Mind mapping.

2. Numerical model and validations

2.1. Model configuration

2.1.1. Engineering background

The design diagram of the PSRW (Fig. 3) adheres to the Chinese specification for the design of rock retaining wall engineering in geological hazards (CAGHP, 2019). The anti-slide piles with a concrete protective layer thickness of 0.04 m have a cross-section area of 1.8 m × 1.25 m. The total pile length is 12 m, and the embedded section is 6 m. The HRB 400 longitudinal bar with diameters of 25 mm and 32 mm were arranged in the pile (Fig. 3c). The stirrups are HRB335 with a diameter of 16 mm and a spacing of 200 mm. The slabs between the piles are 6 m in length, 3.5 m in width, and 0.5 m in thickness. These slabs contain two layers of 16 mm-diameter reinforced bar. The sand buffer layer are 1 m and 5 m on top and bottom, respectively. A geogrid is horizontally placed in the buffer layer at 0.25 m intervals. Lastly, 1 m^3 sphere rock boulder with a diameter of 1.24 m was set as an impactor. The impact locations are 2# slab center (CS) and 3# pile center (CP) at 5.25 m over the ground.

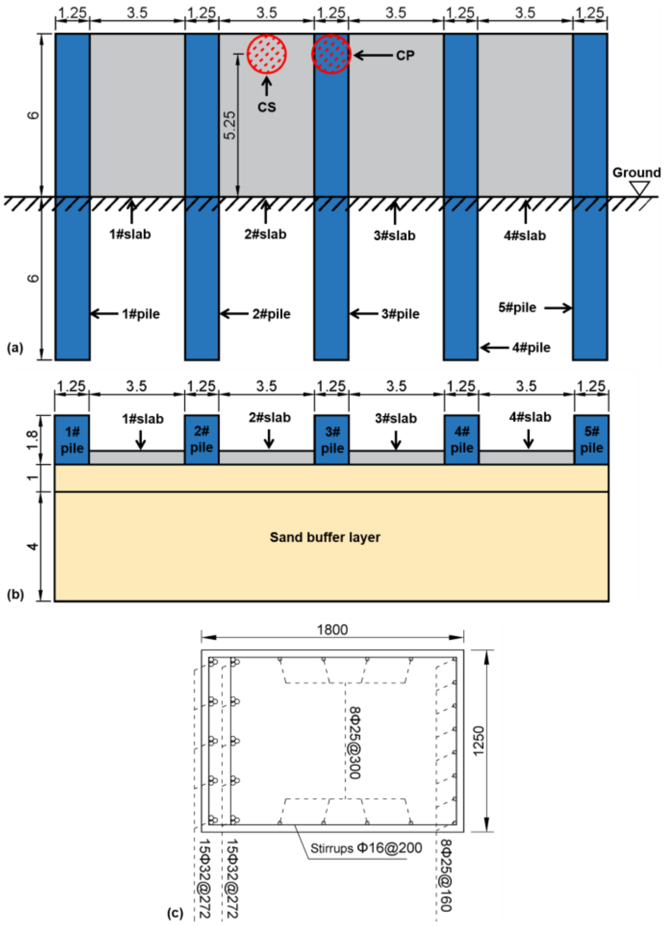

Fig. 3. The design diagram of PSRW (a) front view (unit: m) (b) top view (unit: m) (c) cross-section profile of pile (unit: mm).

2.1.2. *Soil-pile interaction*

Under the impact, the lateral deformations of the pile are greatly influenced by the plastic behavior of the soil, particularly the soil near the pile. Given their importance and complexity, it isn't easy to thoroughly describe soil-pile interactions. This paper calculates the pile-soil interaction by the lateral resistance-deflection (*p*-*y*) curve method. As state by Truong and Lehane (2018), the *p*-*y* curves for square cross-section pile are utilized as

$$\frac{P}{P_{\mathrm{u}}} = \tanh\left[5.45\left(\frac{y}{B}\right)^{0.52}\right] \tag{1}$$

$$\frac{P}{s_{\mathrm{u\_cu}}} = 10.5\left[1 - 0.75e^{-0.6z/B}\right]S_{\mathrm{p}} \tag{2}$$

where P is the actual lateral soil resistance, kPa; P_u is the ultimate lateral soil resistance, kPa; S_{u_cu} is consolidated isotropic undrained triaxial shear strength of soil, kPa/m; y is the actual lateral soil deformation, m; B is pile width, m; z is depth below the soil surface, m; S_p is a shape correction factor.

According to the reference and simulated model, the S_{u_cu} and S_p are adopted as 1.5 kPa/m and 1.25, respectively. Besides, the soil is modeled by compressive inelastic springs, arranged every 0.25 m along the pile height and side (Fig. 4a).

2.1.3. Numerical model and numerical simulation scheme

(1) Numerical model

The numerical model of PSRW is shown in Fig. 4. The material constitutive models, unit types, physical-mechanical parameters, and parameter source for all components are listed in Table 1. The rationality of all material constitutive models and physical mechanics parameters were verified in Section 2.2. The both piles and buffer layers are fixed for the boundary conditions. Additionally, both sides of the buffer layer are blocked by infinitely rigid walls. The contact type between the rockfall, sand buffer layer and pile-slab structure were set to automatic surface-to-surface.

(2) Numerical simulation scheme

According to previous research (Muraishi et al., 2005; Chau et al., 2002), angular velocity of impactor was neglected in numerical simulations, and line velocities were set as 10, 15, 20, 25, and 30 m/s, corresponding to impact energies of 130, 292.5, 520, 812.5, and 1170 kJ (Table 2). The linear velocity is perpendicular to surface of the buffer layer.

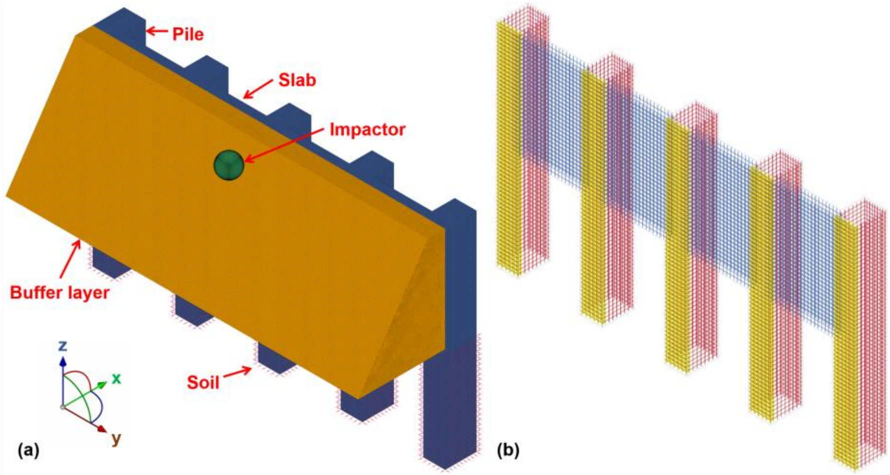

Fig. 4. Numerical model of the PSRW (a) numerical model (b) reinforced bar of PSRW (unit: mm).

Table 1 Material constitutive model and physical-mechanical parameters for various components of PSRW.

Items	Constrained model	Unit types	Integral methods	Density (kg/m^3)	Young's modul (MPa)	Poisson's ratio
Concrete	Continue cap concrete (MAT_159) (Heng et al., 2021)	Solid element	One integration point	2450	30000	0.3
Reinforced bar	Plastic kinematic model (MAT_003) (Heng et al., 2021)	Beam element	2×2 Gauss integration	7850	204000	0.3
Sand buffer layer	Soil-foam model (MAT_063) (Bhatti and Kishi, 2010)	Solid element	One integration point	1720	100	0.3
Impactor	Rigid body (MAT_020)	Solid element	One integration point	2600	20000	0.25
Geogrid	Plastic kinematic model (MAT_003) (Lee et al., 2010)	Shell element	Belytschko-Tsay integration	1030	464	0.3

Table 2 Detailed numerical simulation scheme.

Case	Impact location	Impact height (m)	Impact velocity (m/s)	Impact kinetic energy (kJ)
CP-V10	3# pile center	5.25	10	130
CP-V15			15	292.5
CP-V20			20	520
CP-V25			25	812.5
CP-V30			30	1170
CS-V10	2# slab center		10	130
CS-V15			15	292.5
CS-V20			20	520
CS-V25			25	812.5
CS-V30			30	1170

Note: CP denotes the 3# pile center as impact location; CP denotes the 2# slab center as impact location; V denotes the velocities of rockfall.

2.2. Model validation

In order to verify the rationality of the selected material constitutive model and the established numerical model. Two physical model tests from previously published papers (Heng et al., 2021; Demartino et al., 2017; Schellenberg, 2008) were selected to reproduce.

2.2.1. Failure test of RC cantilever column

The physical model test conducted by Demartino et al. (2017) was selected to verify the ability of constitutive model to reflect the accumulative damage for RC structures under impact loads. The model is composed of a cylindrical column with a diameter of 0.3 m and a height of 1.7 m, and a square-section concrete foundation with length of 0.9 m and height of 0.5 m. The column was reinforced with sixteen 8 mm diameter longitudinal reinforced bar and 6.5 mm diameter stirrups at 100 mm spacing. The foundation was firmly connected to the ground using four 50 mm diameter high-strength prestressed reinforced bar. The experiment involved a test truck made of Q235 steel (considered as a rigid body) (Fig. 5a). The impactor was positioned 0.4 m above the bottom of the column and was released at a velocity of 3.02 m/s (impact energy of 7.21 kJ). Fig. 5b shows the numerical model with hexahedral mesh. The material constitutive models for components are shown in Table 1. For the boundary conditions, the model was fixed with four high-strength bolts.

The trend and amplitude of the impact forces by numerical simulations closely matched the experimental results (Fig. 6). Similarly, Table 3 Simulation results of different mesh sizes.

Items	Impact force (kN)	Displacement of column at 1.2m height (mm)	Number of the element	Computational time (hour)
Physical model test	999.52	22.3	/	/
25 mm mesh size	966.72	23.1	5462900	24
50 mm mesh size	978.1	22	807534	4.2
100 mm mesh size	1009.35	21.3	172268	1.2

Table 4 indicates a consistency between the extent of the experimental and numerical damage in concrete. The deviations of peak impact forces between the numerical simulations and the experiments were below 10% (Table 3). These results suggest that the numerical model and its governing parameters can reliably simulate the accumulative damage in RC structures subjected to impact loads. Considering both accuracy and computational time, a mesh size of 50 mm was selected for the numerical simulations conducted in this study.

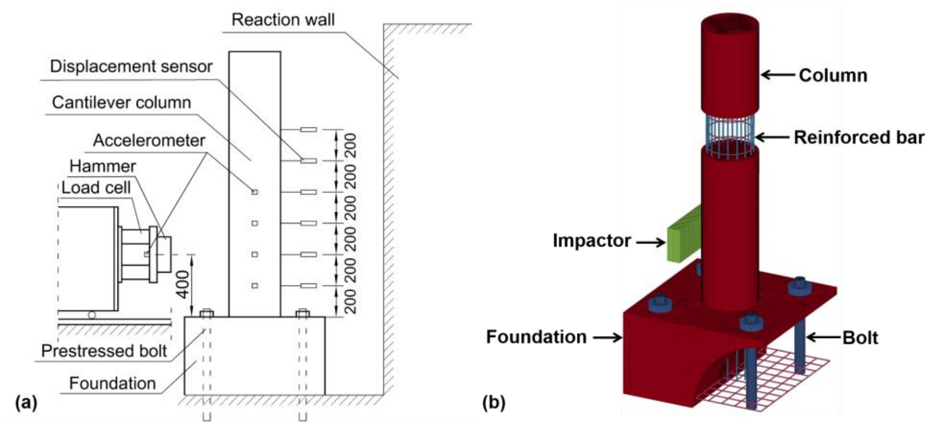

Fig. 5. Model of RC cantilever column failure test
(a) experimental model (b) numerical model (unit: mm).

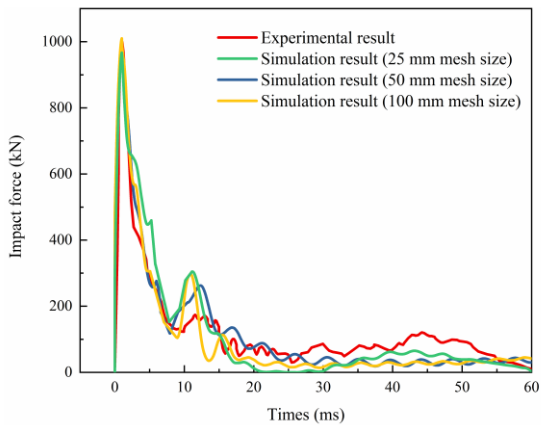

Fig. 6. Dynamic curve of impact force with different mesh size.

Table 3 Simulation results of different mesh sizes.

Items	**Impact force (kN)**	**Displacement of column at 1.2m height (mm)**	**Number of the element**	**Computational time (hour)**
Physical model test	999.52	22.3	/	/
25 mm mesh size	966.72	23.1	5462900	24
50 mm mesh size	978.1	22	807534	4.2
100 mm mesh size	1009.35	21.3	172268	1.2

Table 4 Comparison of experimental and simulation results of concrete damage accumulation with time.

Time(ms)	**7.5**	**10**	**15**	**20**	**50**
Experimental results (Demartino et al., 2017)	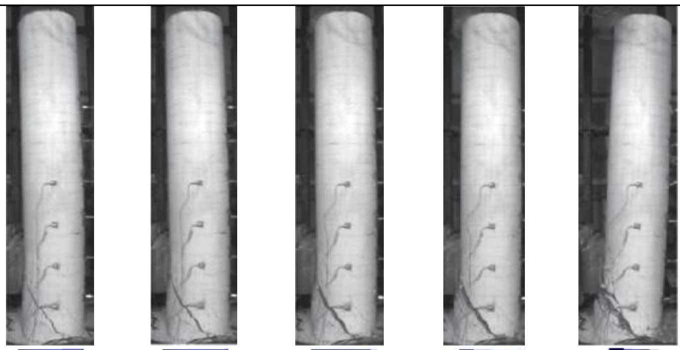				
Simulation results	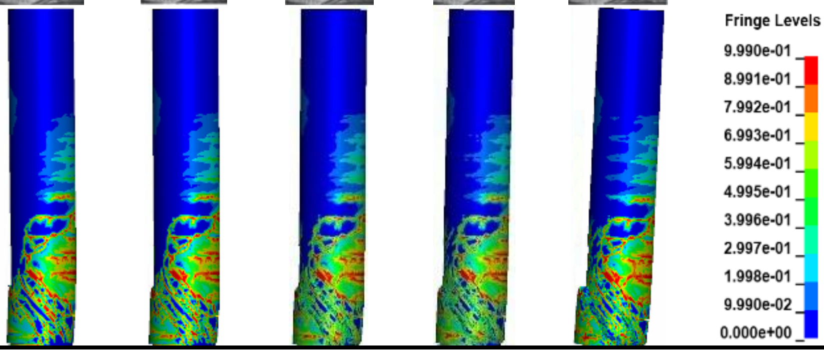				

2.2.2. Failure test of RC slab with a buffer layer

The physical model test conducted by Schellenberg (2008) was selected to validate the capability of the constitutive model to reflect the interaction among the boulder, sand buffer layer, and RC structure. The specimen comprises a RC slab measuring 1.5 m × 1.5 m × 0.23 m and a sand buffer layer with 0.5 m in radius and 0.45m in thickness (Fig. 7). The slab is reinforced with one layer of reinforced bar with 12 mm diameter and a spacing of 95 mm for the lower layer. The diameter and density of the boulder are 0.8 m and 3110 kg/m^3, respectively. The impact position is located at the center of the buffer layer, with an impact velocity of 5.5 m/s (impact energy of 14.4 kJ). The material constitutive models for concrete, reinforced bar, and sand buffer layer are shown in Table 1. For the Boundary conditions, the bottom of the supports was fixed.

Fig. 8 presents the dynamic curve of impact force, displacement of slab center, and axial strain of center reinforced bar. The results demonstrate that the deviations of the peak impact force, the maximum strain of reinforced bar, and the slab center displacement are less than 10%. Therefore, the numerical model and its governing parameters are deemed reliable for simulating the behavior of a sand cushion layer and an RC structure under impact loads.

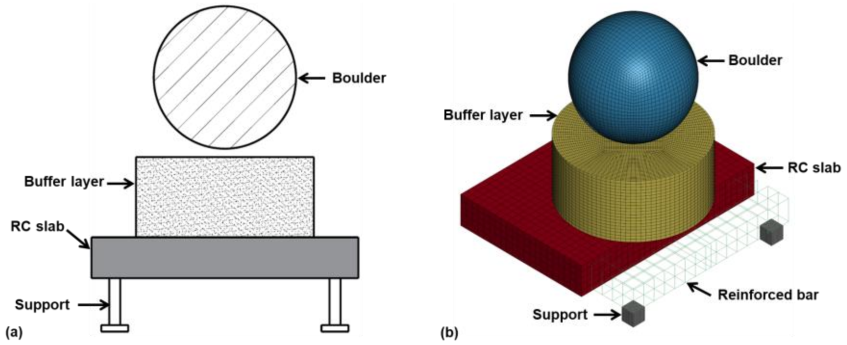

Fig. 7. Model of RC slab failure test
(a) experimental model (b) numerical model (unit: mm).

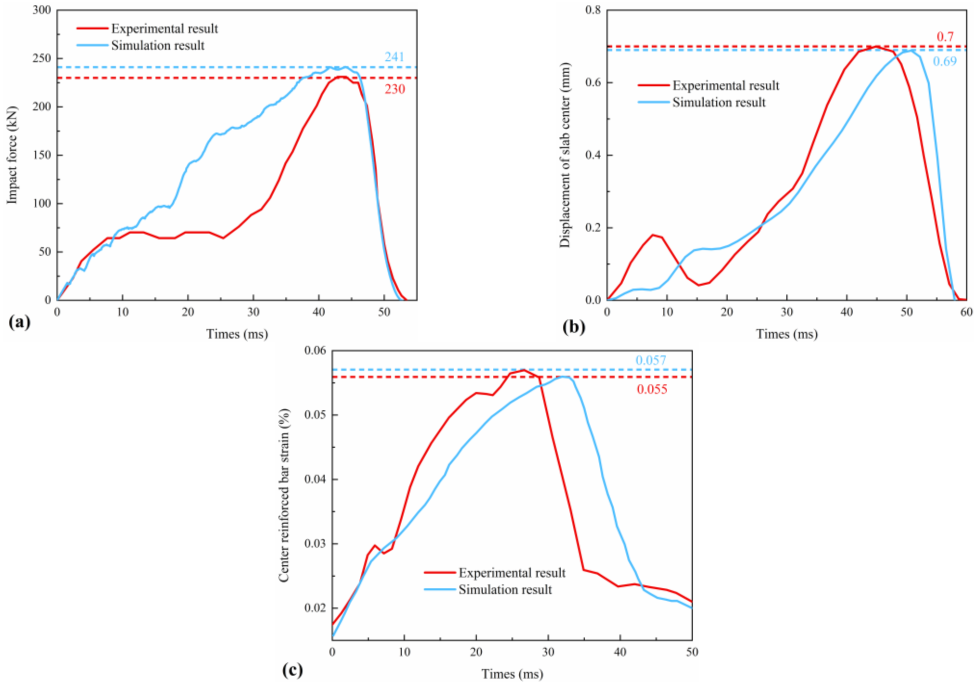

Fig. 8. Comparisons between experimental and simulation results
(a) impact force (b) displacement of slab center (c) axial strain of reinforced bar.

3. Numerical results

In this section, the dynamic response of PSRW under different impact centers and different impact velocities are compared and analyzed. The main evaluation indexes are as follows: impact force (the contact force between the impactor and the buffer layer), interaction force (the contact force between the buffer layer and the RC structure), stress of concrete and reinforced bar, concrete damage, lateral displacement at the crown of different components (piles and slabs), and lateral displacement of all piles at the ground surface.

3.1. *Influence of different impact centers*

To analyze the influence of dynamic behaviors of PSRW under different impact centers, two group simulations under maximum impact energy (CP-V30 and CS-V30) are selected for comparison.

3.1.1. *Impact force and interaction force*

Fig. 9a and 9b show the dynamic curves of the impact force and interaction force, respectively. Both force curves exhibit a distinct single-peaked pattern. The impact force rapidly reduces to zero due to the energy-dissipating properties of the sand buffer layer (Fig. 9a). In contrast, the interaction force remains at a non-zero value (475 kN) (Fig. 9b). Owing to the permanent deformation sustained by the structure, and the gravitational force exerted by the sand buffer acts on the surface of the structure. Furthermore, Fig. 9a illustrates the close overlap of the impact forces for various impact centers, depending on the buffer and impactor characteristics, and minimally affected by the impact center. The slight differences observed in the dynamic curve of interaction force under CP-V30 and CS-V30 may be attributed to the flexural stiffness of the slab and pile.

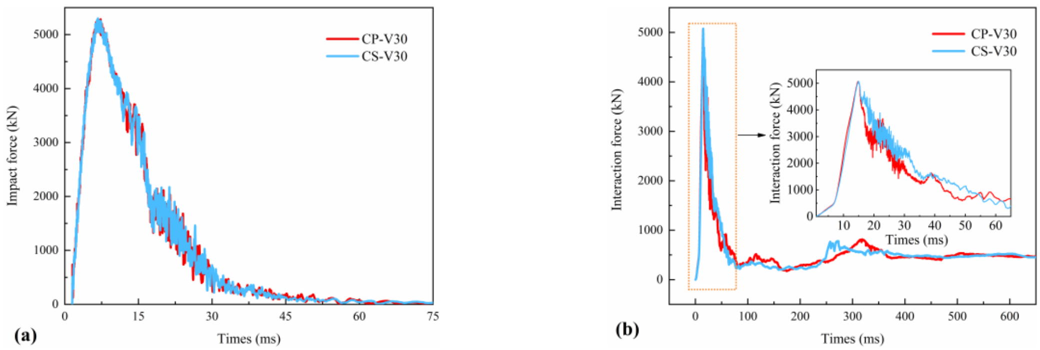

Fig. 9. Dynamic curves of impact force and interaction force under various impact centers (a) impact force (b) interactional force.

3.1.2. *Stress of concrete*

The minimum principal stress of concrete and the effective stress of reinforced bar are important indexes to evaluate the dynamic response of RC structures (Zhong et al., 2021; Zhong et al., 2022). Fig. 10 shows the minimum principal stress nephogram of concrete under CP-V30 from 1 to 650 ms. When t = 1 ms (Fig. 10a), the minimum stress focus on the bottom of the piles. When t = 14.7 ms (Fig. 10b), the minimum principal stress of concrete around the impact point increased rapidly to 7.421 MPa. When t= 22.8 ms (Fig. 10c), the concrete elements at the joints of the 3# pile and slabs achieve compressive strength, leading to concrete damage. When t= 650 ms (Fig. 10d), the total volume of damaged elements reaches 0.63 m^3, which occupies a proportion of 0.35%.

Fig. 11 shows the minimum principal stress nephogram of concrete under CP-V30 from 1 to 650 ms. When t = 1 ms, the maximum stress focus on the bottom of the piles (Fig. 11a). When t = 14.7 ms, the minimum principal stress around the impact point increased rapidly to 12.117 MPa (Fig. 11b). When t = 22.4 ms, the elements of the concrete at the impact point of the 2# slab achieve ultimate compressive strength, leading to the concrete damage (Fig. 11c). When t = 650 ms, the total volume of damage elements reaches 0.61 m^3 (Fig. 11d), which occupies a proportion of 0.34%.

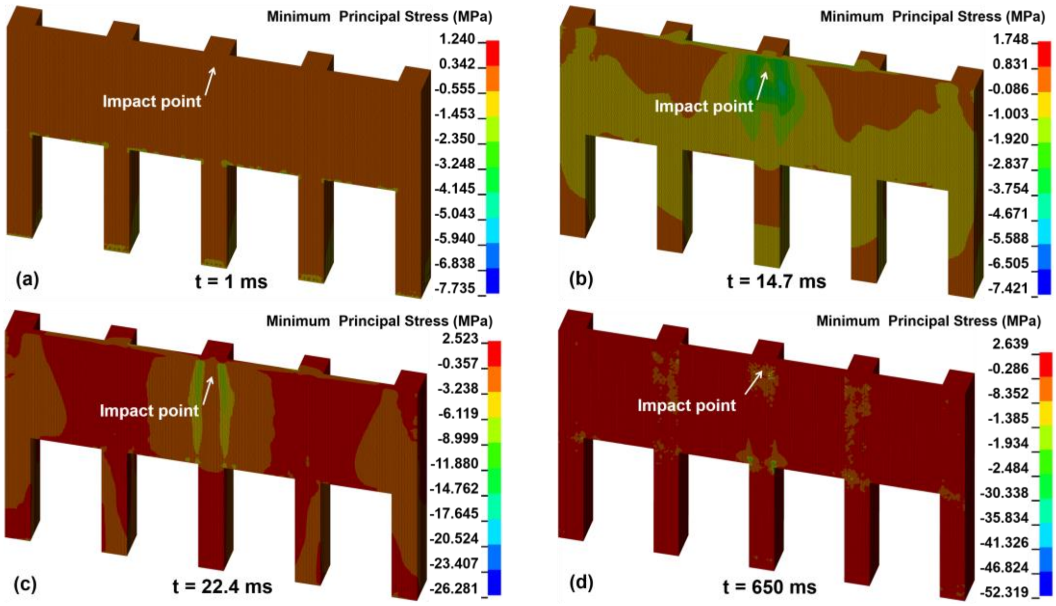

Fig. 10. Minimum principal stress nephogram of concrete under CP-V30.

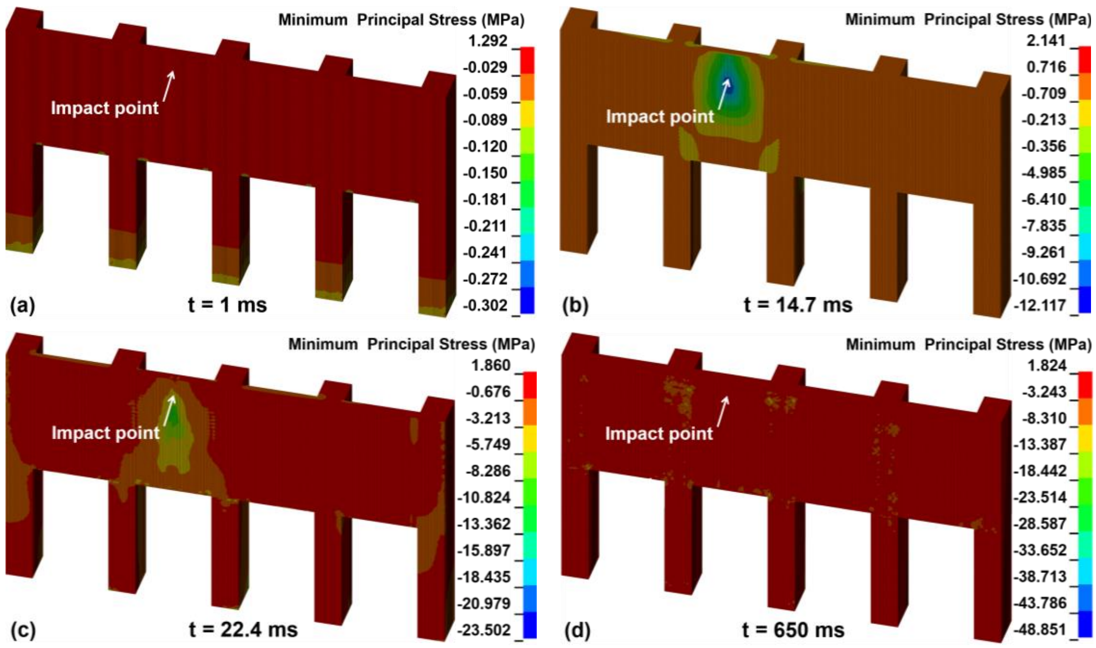

Fig. 11. Minimum principal stress nephogram of concrete under CS-V30.

3.1.3. *Stress of reinforced bar*

Fig. 12 shows the effective stress nephogram of the reinforced bar from 1 to 650 ms under the condition of CP-V30. It can be observed that: (i) when t = 1 ms, the maximum stress concentrated at the bottom of the pile (Fig. 12a); (ii) when t = 14.7 ms (the moment of attaining the maximum interaction force), the maximum stress concentrated at the vicinity of the impact point and the joints of piles and slabs (Fig. 12c); (iii) when t = 650 ms, the maximum stress concentrated at the longitudinal bar of 2#, 3#, and 4# pile (Fig. 12d). Noteworthily, the effective stress of reinforced bar did not exceed the ultimate yield stress.

Fig. 13 shows the effective stress nephogram of reinforced bar from 1 to 650 ms under CS-V30. It can be observed that: (i) when t = 1 ms, the maximum stress concentrated at the bottom of the pile (Fig. 13a); (ii) when t = 14.7 ms, the effective stress of reinforced bar around the impact point increased rapidly to 137.2 MPa (Fig. 13c); (iii) when t = 650 ms, the maximum stress concentrated at the longitudinal bar of 2#, 3#, and 4# pile (Fig. 13d). Noteworthily, the effective stress of reinforced bar did not exceed the ultimate yield stress.

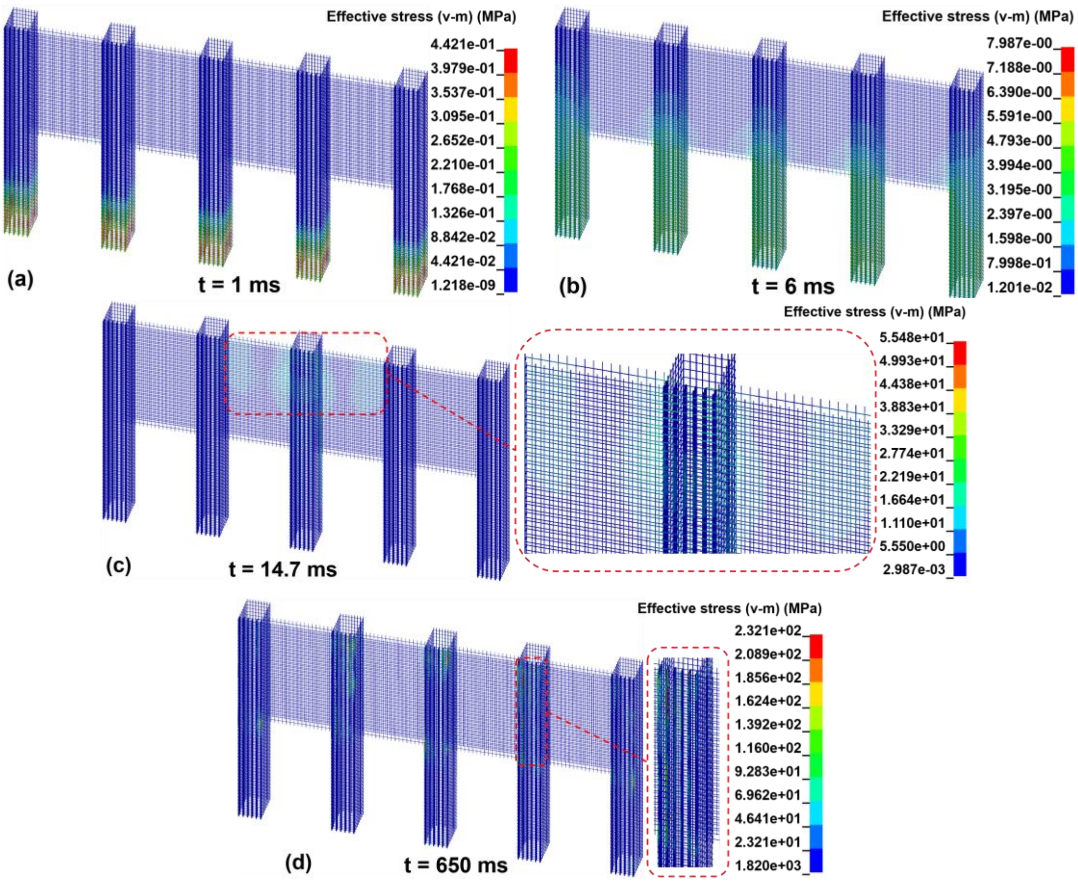

Fig. 12. Effective stress nephogram of reinforced bar under CP-V30.

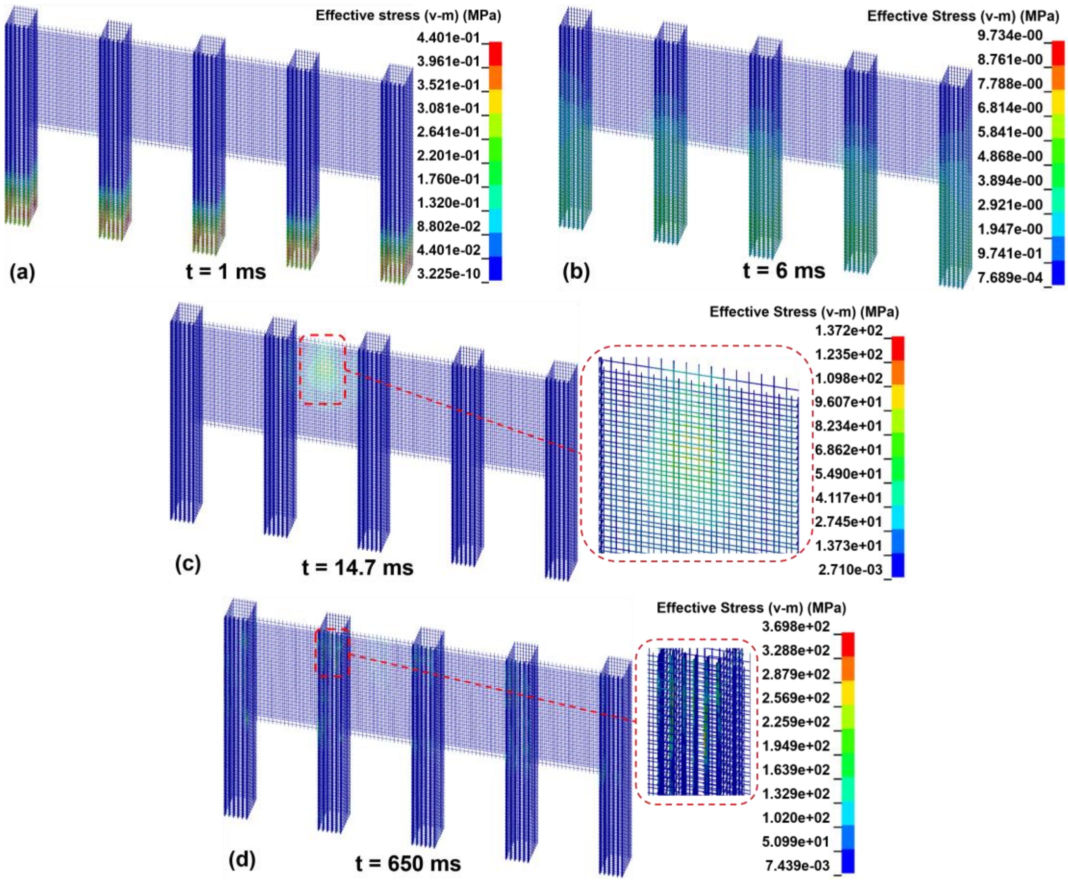

Fig. 13. Effective stress nephogram of reinforced bar under CS-V30.

3.1.4. Lateral displacement at the crown of different components

Fig. 14a presents lateral displacements at the crown of different components under CP-V30 and CS-V30 conditions. The lateral displacement rapidly increased till t = 177 ms and gradually decreased until t = 650 ms. The final displacement does not reach 0, indicating plastic deformation of both the pile and the slab. Comparing the lateral displacement under CS-V30 and CP-V30 (Fig. 14), the trends are consistent, but the magnitude differs. This discrepancy in magnitude can be attributed to the greater deformation capacity of slab compared to pile when subjected to the same impact energy.

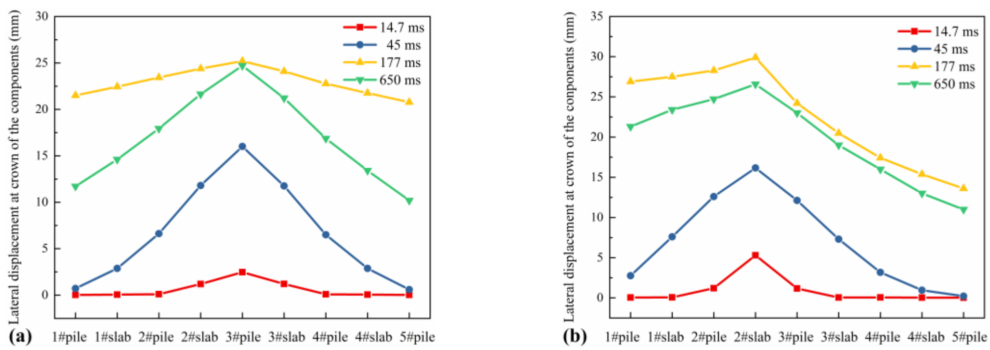

Fig. 14. Lateral displacement at crown of the components (a) CP-V30 (b) CS-V30.

3.1.5. Lateral displacement of piles at the ground surface

Fig. 15a and 16b show the dynamic curve of lateral displacement of all piles at the ground surface under CP-V30 and CS-V30, respectively. Under CP-V30, the 3# pile exhibited the maximum lateral displacement, whereas the 2# pile exhibited the maximum lateral displacement under CS-V30. This discrepancy is due to the structural asymmetry on either side of the impact center under CS-V30, which allows one side of pile #2 greater freedom, resulting in larger lateral displacement. When comparing the lateral displacement of 2# pile under CS-V30 and 3# pile under CP-V30 (Fig. 15c), it is apparent that the maximum lateral displacement of pile at the ground surface is greater under CP conditions, despite the same impact velocity. The characteristics of the lateral displacements suggest that the concrete slab is capable of undergoing larger deformations and absorbing more energy.

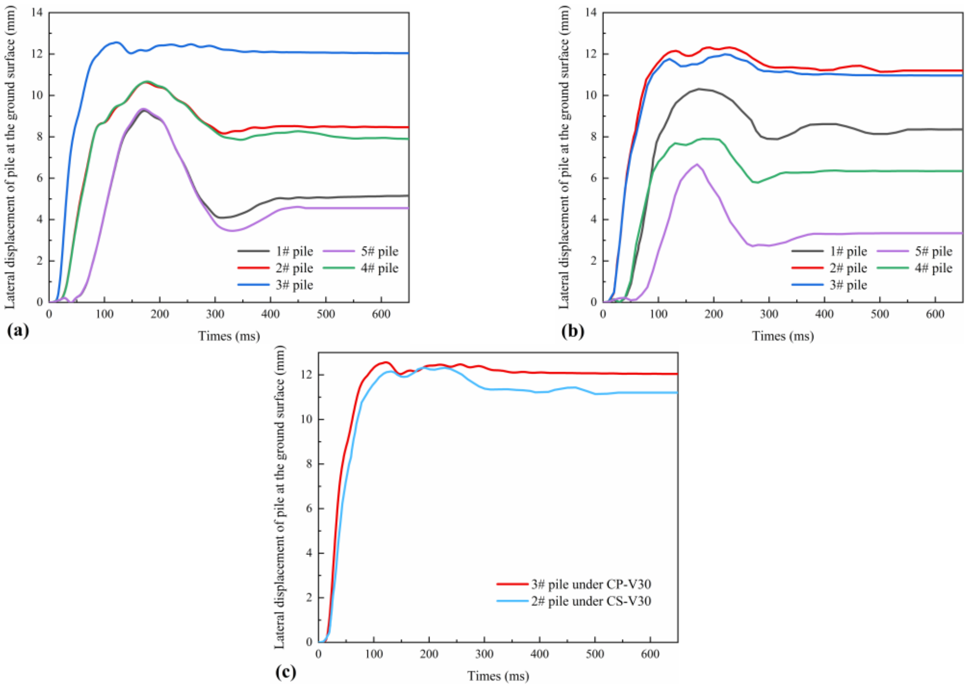

Fig. 15. Dynamic curves of lateral displacement of pile at the ground surface
(a) CP-V30 (b) CS-V30 (c) compare between CP-V30 and CS-V30.

3.2. Influence of different impact velocities

Figure 17 demonstrates that under CP conditions, the impact force, interaction force, and lateral displacement of pile #3 at the ground surface increase as the impact velocity of rockfall rises. When the velocity increases from 15 m/s to 30 m/s, the impact force increases by 1.42, 1.91, and 2.41 times, the interaction force increases by 1.25, 1.47, and 1.68 times, and the lateral displacement of 3# pile at ground surface increases by 1.57, 2.24, and 3 times at t = 650 ms.

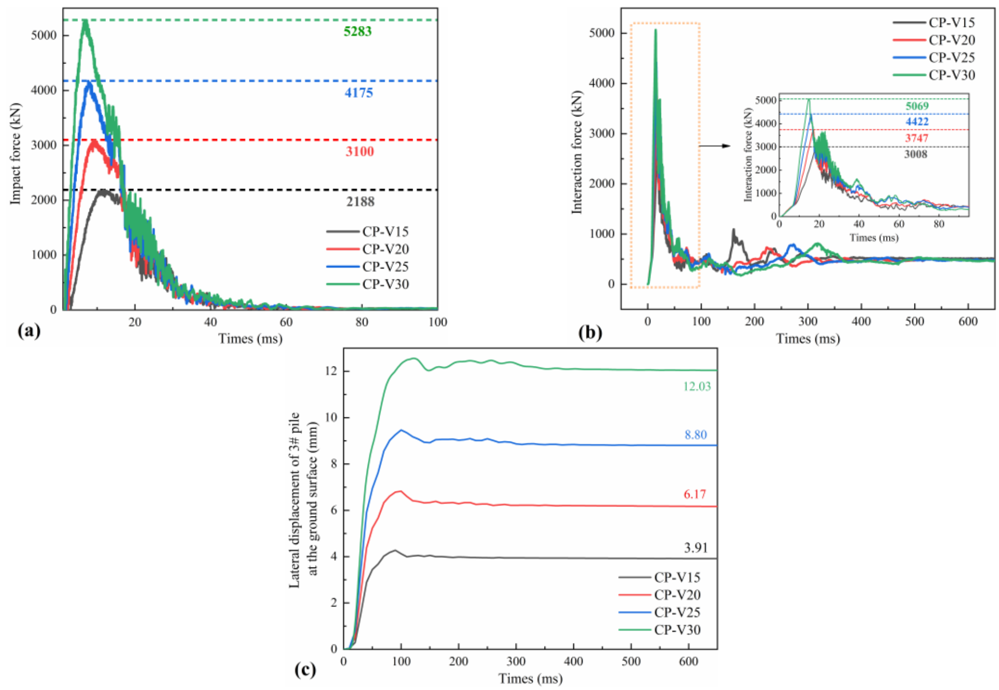

Fig. 16. Dynamic curves of evaluation indexes under various velocities
(a) impact force (b) interactional force (c) lateral displacement at the ground surface of 3# pile.

Fig. 17 shows the impact force, interaction force, and lateral displacement of 2# pile at the ground surface enlarge as the impact velocity increases under CS conditions. When the velocity increases from 15 m/s to 30 m/s, the impact force increases by 1.41, 1.90, and 2.41 times, the interaction force increases by 1.24, 1.47, and 1.68 times, and the lateral displacement of 3# pile at ground surface increases by 1.55, 2.23, and 3 times at t = 650 ms.

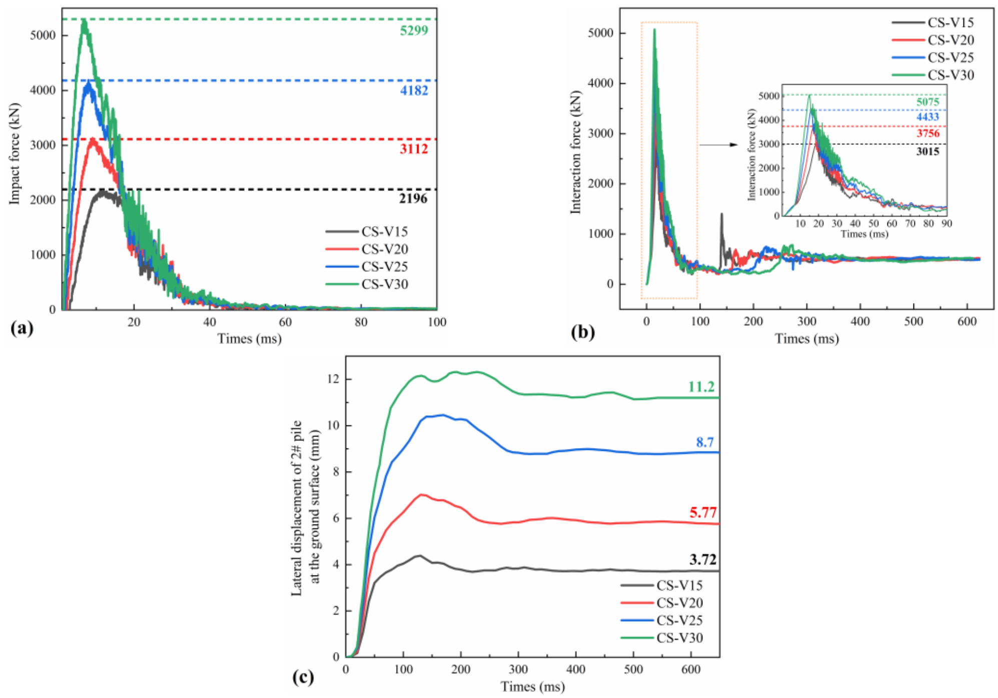

Fig. 17. Dynamic curves of evaluation indexes under various velocities
(a) impact force (b) interactional force (c) lateral displacement at the ground surface of 3# pile.

4. Discussions

4.1. *Comparison of impact force calculation models*

A comparative analysis compared the elastic theories proposed by Labiouse et al. (1996), Kawahara and Muro (2006), Pichler et al. (2006), and Hertz (1881) was conducted to assess the validity of the numerical simulation (Fig. 18). The results reveal a fundamental linear correlation between impact force and velocity. Overall, the computational results are consistent with those of other models in terms of magnitude, thus confirming the validity of the calculations reported here.

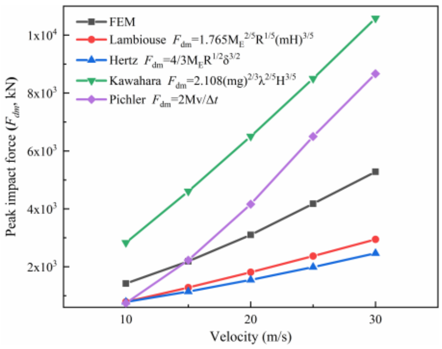

Fig. 18. Relationship between impact velocity and impact force.

4.2. *Relationship between structural evaluation indexes and impact energy*

Table 5 lists the initial kinetic energy of impactor (E), the peak impact force (F_{dm}), the peak interaction force (F_{im}), the ratio of the peak impact force to the peak interaction force (α), the maximum the lateral displacement of pile at the ground surface at t = 650 ms (S_{mpt}), the number of damage failure units (N_d), and the ratio of damage failure units to overall RC structure units (β).

Table 5 Simulation results of various impact cases.

Case	E (kJ)	F_{dm} (kN)	F_{im} (kN)	α (%)	S_{mpt} (mm)	N_d	β (%)
CP-V10	130	1420	2170	65.4	2.25	83	0.0059
CP-V15	292.5	2188	3008	72.7	3.91	817	0.0577
CP-V20	520	3100	3747	82.7	6.17	2179	0.1539
CP-V25	812.5	4175	4422	94.4	8.8	3088	0.2181
CP-V30	1170	5283	5069	104.2	12.03	5040	0.3559
CS-V10	130	1426	2182	65.4	1.76	52	0.0037
CS-V15	292.5	2196	3015	72.7	3.72	321	0.0227
CS-V20	520	3112	3756	82.7	5.77	1062	0.0750
CS-V25	812.5	4182	4433	94.4	8.7	2728	0.1927
CS-V30	1170	5299	5075	104.2	11.2	4880	0.3446

Under the premise of known impact energy, estimating impact force, interaction force, and displacement of pile for the structural design is very important. As shown in Table 5, the variation in peak impact force (F_{dm}) with different impact centers is minimal. Consequently, CP simulation results were chosen for further analysis. The dependence of the peak impact force on the impact energy is shown in Fig. 19a, with a correlation coefficient R^2 = 0.99, i.e.,

$$F_{dm} = 3.69(E + 290.33) = 1845(mv^2 + 0.58) \quad (1)$$

where m is the impactor mass (m= 2600 kg herein); v is the initial impact velocity (10 m/s ⩽ v ⩽ 30 m/s herein).

The dependence of the ratio of peak impact force to peak interaction force on the impact energy is shown in Fig. 19b, with a correlation coefficient of 0.99, i.e.,

$$\alpha = 0.037(E + 1671.89) = 18.5(mv^2 + 3.34) \quad (2)$$

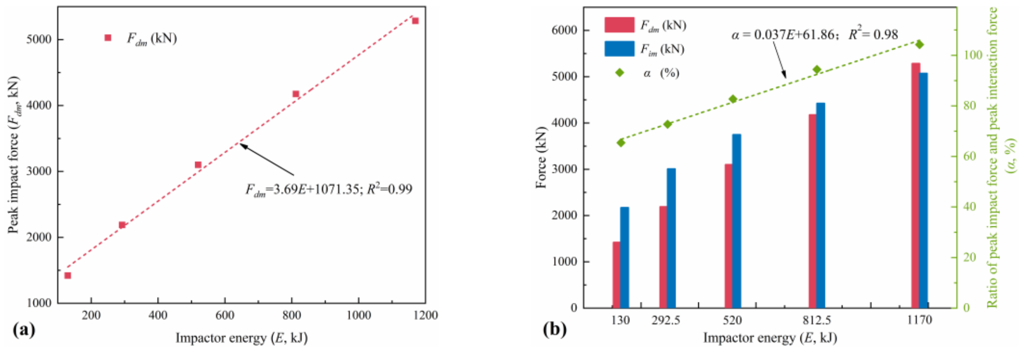

Fig. 19. Dependence of various indexes on impactor energy (a) peak impact force (b) the ratio of peak impact force and peak interaction force.

The lateral displacement of pile at the ground surface is an important index to judge the failure of pile foundation under lateral load. As shown in Table 5, the maximum lateral displacement of pile at the ground surface under pile as impact center is greater than that under slab as impact center. Therefore, the situation where the pile is the center of impact is the more dangerous. As shown in Fig. 20, with the increase of impact energy, the displacement value and number of damage failure units enlarges, which means the structure suffers more damage under CP. Furthermore, the maximum lateral displacement of pile at the ground surface when t = 650 ms, can be calculated by the following aquation:

$$S_{mpt} = 0.00934\left(E + 164.88\right) = 4.67\left(mv^2 + 0.33\right) \quad (3)$$

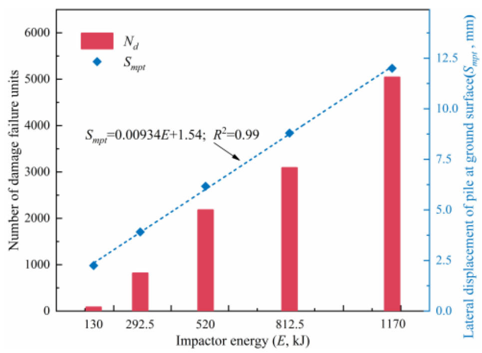

Fig. 20. Dependence of the lateral displacement of 3# pile at the ground surface on impactor energy

According to the Chinese Specification for the Design of Rock Retaining Wall Engineering in Geological Hazards (CAGHP, 2019), the lateral displacement of the resistant sliding pile at the ground surface must not exceed 10 mm. Substituting this value into Formula 3, the maximum impact energy that the PSRW can withstand in this study is 905 kJ.

4.3. Comparison with other concrete rockfall retaining walls

Table 6 presents crucial data on an improved cast-in-place rockfall concrete barrier developed by the US Department of Transportation (Patnaik et al., 2015). This barrier exhibits relatively low resistance to impact energy, which restricts its applicability to situations where high-impact energy rockfalls are likely to occur. Integrating a specialized buffering layer on the concrete retaining wall, the barrier's impact resistance can be effectively enhanced (Kurihashi et al., 2020). According to Maegawa et al. (2011), concrete rockfall barriers with a buffering layer offer a maximum impact resistance ranging from approximately 120 to 490 kJ. Addressing the resistance limitations of traditional concrete rockfall barriers, Furet et al. (2022) proposed the articulated concrete block rockfall protection structures. These innovative structures allow concrete blocks hingedly connected to one another, enabling greater impact energy absorption.

Table 6 Comparison of different concrete rockfall protection structures

Structure name	The maximum impact energy that structure can withstand (kJ)	Energy dissipation ratio (%)	Interception altitude (m)
Cast-in-place rockfall concrete barriers (Patnaik et al., 2015)	127	/	0.81
Concrete retaining wall with buffering system (Kurihashi et al., 2020)	273	100	2.5
Concrete rock – wall (Maegawa et al., 2011)	490	/	/
Articulated concrete blocks rockfall protection structure (Furet et al., 2022)	1020	100	3.2
Pile-slab retaining wall	905	100	6

Note: Energy dissipation ratio denotes the ratio of dissipated energy to input energy.

In terms of energy dissipation, structure damage and friction are responsible for 74% of the impact energy dissipation, with the remaining 26% attributed to other phenomena such as deformation of structural elements, elastic wave propagation, viscous damping, and fracturing. Compared to conventional concrete rockfall barriers, PSRW exhibit significantly higher impact resistance (905 kJ) and interception height (6 m). Similarly, these structures absorb all the impact energy, preventing the impactor from rebounding.

For traditional RC retaining walls subjected to a 16 kJ impact energy, shear cracks develop diagonally from the impact point, with wider spreading observed on the rear face compared to the collision surface (Kurihashi et al., 2020). Fig. 21 illustrates the concrete damage nephogram of PSRW under the impact load of 1170 kN. It is evident that concrete damage primarily concentrated around the impact point and at the junction between the pile and slab. Importantly, there is no evidence of crack penetration into the structure itself, indicating that the PSRW maintains its structural integrity.

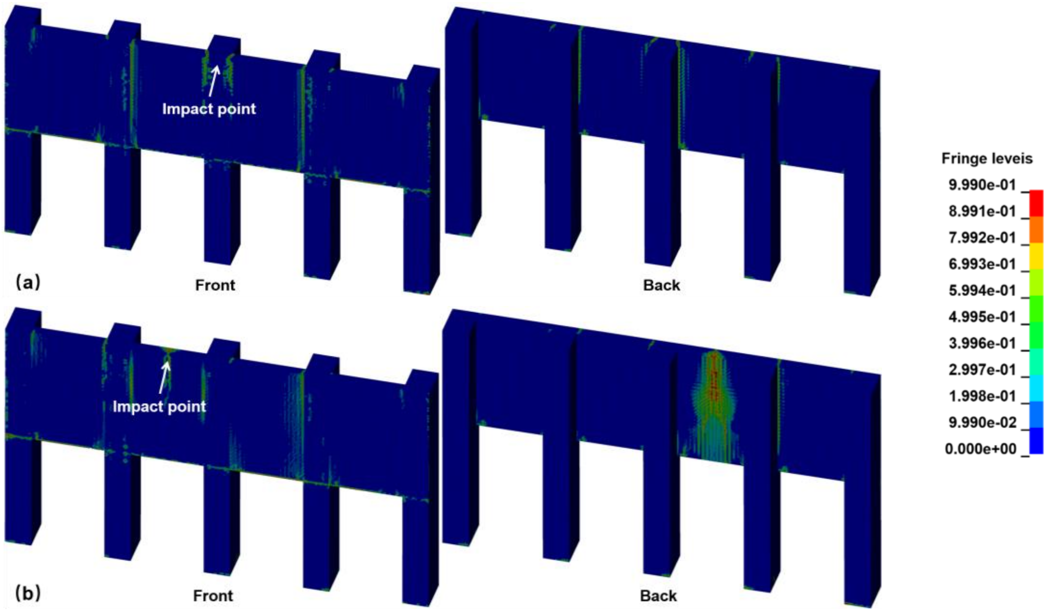

Fig. 21. Damage nephogram of concrete at t = 650 ms (a) CP-V30 (b) CS-V30.

Although the lateral displacement of the pile exceeds the stipulated limit, reaching 12mm as indicated in Table 5 and Figure 21, it is essential to recognize that the specified ultimate lateral displacement is often a conservative estimate. Concurrently, the maximum lateral displacement at the crown of the cantilever section is 35 mm, which is substantially less than the lateral displacement threshold for the cantilever section of the anti-slide pile. This threshold is defined as 1% of the cantilever section's length, according to CAGHP (2019). As a result, the impact load does not compromise the integrity of the structure.

In summary, the PSRW is an innovative rockfall protection structure, providing an enhanced level of impact resistance, increased interception height, and reduced concrete damage. Additionally, the minimal lateral displacement observed after impact further ensures the structural integrity and safety in challenging terrain areas.

4.4. Discussion on Engineering Practicality

The data presented in Table 7 reveal the distribution of rockfall energy levels across four regions that experience frequent rockfalls. It is evident from the table that substantial rockfalls with an impact energy of less than 1000 kJ occur in the Alps region. Schneider et al. (2023) utilized Doppler radar technology to monitor rockfall activity in Brienz/Brinzals, Switzerland. Their research indicated that although the volume of rockfalls ranged from 1 to 100 m^3, smaller events (1 m^3) were significantly more prevalent. As previously mentioned, the PSRW demonstrates resistance against rockfalls with an impact energy of approximately 1000 kJ, thereby rendering it an appropriate choice for numerous small alpine rockfall scenarios. Additionally, its compact size and robust structural stability enhance its suitability for mountainous construction.

Table 7 Rockfall events in different areas

Study area	Total number of rockfall events	Rockfall energy < 1000 kJ	Percentage
French Alps (Le Roy et al., 2019)	18	9	50%
Swiss Alps (Dietze et al., 2017)	37	37	100%
Along the railway in Japan (Muraishi et al., 2005)	173	158	91%
New South Wales, Australia (Spadari et al., 2013)	211	200	94%

5. Conclusion

Numerical experiments of PSRW under 1 m^3 boulder impact were performed to comprehensively analyze the impact force, interaction force, stress of concrete and reinforced bars, concrete damage, and the lateral displacements of components. The main conclusions are as follows:

(1) The impact force exhibits a linear correlation with velocity. In comparison to several classical models for calculating impact force, the results obtained in this study are of the same order of magnitude as those derived from other models under analogous conditions.

(2) Concrete damage mainly concentrates at the joints between piles and slabs, the impact center, and the section of piles at the ground surface. To reduce structural concrete damage, these critical sections should be initially considered in structural optimization efforts.

(3) Under various impact center conditions, the difference of impact force and interaction force is very small. However, when the pile serves as the impact center, lateral displacement of pile at the ground surface and concrete damage are significantly greater. This indicates that having the pile as the impact center represents a more hazardous impact scenario.

(4) Principal structural evaluation indexes, including the impact force, the ratio of the peak impact force to the peak interaction force, and the maximum lateral displacement of the pile at the ground surface, increase with the growth of impact energy. These relationships are instrumental for assessing impact forces, interaction forces, and the lateral displacement of piles at ground surface during the design of PRSW structures. According to the correlation between the impact energy and lateral displacement of pile at the ground surface, the maximum impact energy that the PSRW, which while satisfies the displacement requirements of Chinese specifications, can withstand is 905 kJ when the structure's crown is designated as the impact point.

(5) In comparison to existing rockfall protection structures, the PSRW exhibits superior stability and occupies a reduced footprint. Furthermore, this structure is capable of addressing a wide range of rockfall impact scenarios commonly encountered in alpine canyon regions.

CRediT authorship contribution statement

Peng Zou: Methodology, Simulation, Visualization, Writing - original draft. **Gang Luo:** Tests design, funding acquisition, writing - review. **Yuzhang Bi:** Visualization, Writing - review. **Hanhua Xu:** Writing - review.

Declaration of Competing Interest

The authors declare that they have no known competing financial interests or personal relationships that could have appeared to influence the work reported in this paper.

Acknowledgments

This research was funded by the National Natural Science Foundation of China (42277143), the National Key R&D Program of China (2022YFC3005704), the Sichuan Province Science and Technology Support Program (24NSFSC2303) and the Science and the research project of the Department of Natural Resources of Sichuan Province (KJ-2023-004, KJ-2023-029). The authors also thank the editors and anonymous reviewers for their constructive comments that improved the manuscript.

References

Bhatti, A. Q. and Kishi, N.: Impact response of RC rock-shed girder with sand cushion under falling load, Nuclear Engineering and Design, 240, 2626-2632, https://doi.org/10.1016/j.nucengdes.2010.07.029, 2010.

Bi, Y., Li, M., Wang, D., Zheng, L., Yan, S., and He, S.: A numerical study of viscous granular flow in artificial step-pool systems: flow characteristics and structure optimization, Acta Geotechnica, https://doi.org/10.1007/s11440-023-01933-1, 2023.

CAGHP: Code for design of rock retaining wall engineering in geological hazards (T/CAGHP060-2019), China University of Geosciences Press, Wuhan2019. (in Chinese)

Chau, K. T., Wong, R., and Wu, J.: Coefficient of restitution and rotational motions of rockfall impacts, International Journal of Rock Mechanics and Mining Sciences, 39, 69-77, https://doi.org/10.1016/S1365-1609(02)00016-3, 2002.

Crosta, G. and Agliardi, F.: Parametric evaluation of 3D dispersion of rockfall trajectories, Natural Hazards and Earth System Sciences, 4, 583-598, https://doi.org/10.5194/nhess-4-583-2004, 2004.

Demartino, C., Wu, J. G., and Xiao, Y.: Response of shear-deficient reinforced circular RC columns under lateral impact loading, International Journal of Impact Engineering, 109, 196-213, https://doi.org/10.1016/j.ijimpeng.2017.06.011, 2017.

Dietze, M., Mohadjer, S., Turowski, J. M., Ehlers, T. A., and Hovius, N. J. E. S. D.: Seismic monitoring of small alpine rockfalls–validity, precision and limitations, 5, 653-668, 2017.

Fan, W., Zhong, Z., Huang, X., Sun, W., and Mao, W.: Multi-platform simulation of reinforced concrete structures under impact loading, Engineering Structures, 266, 114523, https://doi.org/10.1016/j.engstruct.2022.114523, 2022.

Furet, A., Villard, P., Jarrin, J.-P., and Lambert, S.: Experimental and numerical impact responses of an innovative rockfall protection structure made of articulated concrete blocks, Rock Mechanics and Rock Engineering, 55, 5983-6000, https://doi.org/10.1007/s00603-022-02957-x, 2022.

Heng, K., Li, R., Li, Z., and Wu, H.: Dynamic responses of highway bridge subjected to heavy truck impact, Engineering Structures, 232, 11828-11850, https://doi.org/10.1016/j.engstruct.2020.111828, 2021.

Hertz, H.: The contact of elastic solids, J Reine Angew, Math, 92, 156-171, 1881.

Hu, X., Mei, X., Yang, Y., and Luo, G.: Dynamic Response of Pile-plate Rock Retaining Wall under Impact of Rockfall, Journal of Engineering Geology, 27, 123-133, 2019. (in Chinese)

Hungr, O., Leroueil, S., and Picarelli, L.: The Varnes classification of landslide types, an update, Landslides, 11, 167-194, https://doi.org/10.1007/s10346-013-0436-y, 2014.

Kawahara, S. and Muro, T.: Effects of dry density and thickness of sandy soil on impact response due to rockfall, Journal of terramechanics, 43, 329-340, https://doi.org/10.1016/j.jterra.2005.05.009, 2006.

Kurihashi, Y., Oyama, R., Komuro, M., Murata, Y., and Watanabe, S.: Experimental study on buffering system for concrete retaining walls using geocell filled with single-grain crushed stone, International Journal of Civil Engineering, 18, 1097-1111, https://doi.org/10.1007/s40999-020-00520-9, 2020.

Labiouse, V., Descoeudres, F., and Montani, S.: Experimental study of rock sheds impacted by rock blocks, Structural Engineering International, 6, 171-176, https://doi.org/10.2749/101686696780495536, 1996.

Lambert, S., Gotteland, P., and Nicot, F.: Experimental study of the impact response of geocells as components of rockfall protection embankments, Natural Hazards and Earth System Sciences, 9, 459-467, https://doi.org/10.5194/nhess-9-459-2009, 2009.

Le Roy, G., Helmstetter, A., Amitrano, D., Guyoton, F., and Le Roux-Mallouf, R.: Seismic analysis of the detachment and impact phases of a rockfall and application for estimating rockfall volume and free-fall height, 124, 2602-2622, https://doi.org/10.1029/2019JF004999, 2019.

Lee, K., Chang, N., and Ko, H.: Numerical simulation of geosynthetic-reinforced soil walls under seismic shaking, Geotextiles and Geomembranes, 28, 317-334, https://doi.org/10.1016/j.geotexmem.2009.09.008, 2010.

Lu, L., Lin, H., Wang, Z., Xiao, L., Ma, S., and Arai, K.: Experimental and numerical investigations of reinforced soil wall subjected to impact loading, Rock Mechanics and Rock Engineering, 54, 5651-5666, https://doi.org/10.1007/s00603-021-02579-9, 2021.

Maegawa, K., Yokota, T., and Van, P. T.: Experiments on rockfall protection embankments with geogrids and cushions, GEOMATE Journal, 1, 19-24, 2011.

Mavrouli, O., Giannopoulos, P., Carbonell, J. M., and Syrmakezis, C.: Damage analysis of masonry structures subjected to rockfalls, Landslides, 14, 891-904, https://doi.org/10.1007/s10346-016-0765-8, 2017.

Muraishi, H., Samizo, M., and Sugiyama, T.: Development of a flexible low-energy rockfall protection fence, Quarterly Report of RTRI, 46, 161-166, https://doi.org/10.2219/rtriqr.46.161, 2005.

Patnaik, A., Musa, A., Marchetty, S., and Liang, R.: Full-scale testing and performance evaluation of rockfall concrete barriers, Transportation research record, 2522, 27-36, https://doi.org/10.3141/2522-03, 2015.

Peila, D. and Ronco, C.: Design of rockfall net fences and the new ETAG 027 European guideline, Natural Hazards and Earth System Sciences, 9, 1291-1298, https://doi.org/10.5194/nhess-9-1291-2009, 2009.

Peila, D., Oggeri, C., and Castiglia, C.: Ground reinforced embankments for rockfall protection: design and evaluation of full scale tests, Landslides, 4, 255-265, https://doi.org/10.1007/s10346-007-0081-4, 2007.

Perera, J. S., Lam, N., Disfani, M. M., and Gad, E.: Experimental and analytical investigation of a RC wall with a gabion cushion subjected to boulder impact, International Journal of Impact Engineering, 151, 103823-103839, https://doi.org/10.1016/j.ijimpeng.2021.103823, 2021.

Pichler, B., Hellmich, C., Mang, H. A., and Eberhardsteiner, J.: Loading of a gravel-buried steel pipe subjected to rockfall, Journal of Geotechnical and Geoenvironmental Engineering, 132, 1465-1473, https://doi.org/10.1061/(ASCE)1090-0241(2006)132:11(1465), 2006.

Schellenberg, K.: On the design of rockfall protection galleries, ETH Zurich, 2008.

Schneider, M., Oestreicher, N., Ehrat, T., and Loew, S.: Rockfall monitoring with a Doppler radar on an active rockslide complex in Brienz/Brinzauls (Switzerland), 23, 3337-3354, https://doi.org/10.5194/nhess-23-3337-2023, 2023.

Shen, W., Zhao, T., Dai, F., Jiang, M., and Zhou, G. G.: DEM analyses of rock block shape effect on the response of rockfall impact against a soil buffering layer, Engineering Geology, 249, 60-70, https://doi.org/10.1016/j.enggeo.2018.12.011, 2019.

Spadari, M., Kardani, M., De Carteret, R., Giacomini, A., Buzzi, O., Fityus, S., and Sloan, S.: Statistical evaluation of rockfall energy ranges for different geological settings of New South Wales, Australia, 158, 57-65, https://doi.org/10.1016/j.enggeo.2013.03.007, 2013.

Truong, P. and Lehane, B.: Effects of pile shape and pile end condition on the lateral response of displacement piles in soft clay, Géotechnique, 68, 794-804, https://doi.org/10.1680/jgeot.16.P.291, 2018.

Volkwein, A., Schellenberg, K., Labiouse, V., Agliardi, F., Berger, F., Bourrier, F., Dorren, L. K., Gerber, W., and Jaboyedoff, M.: Rockfall characterisation and structural protection–a review, Natural Hazards and Earth System Sciences, 11, 2617-2651, https://doi.org/10.5194/nhess-11-2617-2011, 2011.

Wu, J., Ma, G., Zhou, Z., Mei, X., and Hu, X.: Experimental Investigation of Impact Response of RC Slabs with a Sandy Soil Cushion Layer, Advances in Civil Engineering, 2021, 1-18, https://doi.org/10.1155/2021/1562158, 2021.

Yang, J., Duan, S., Li, Q., and Liu, C.: A review of flexible protection in rockfall protection, Natural Hazards, 99, 71-89, https://doi.org/10.1007/s11069-019-03709-x, 2019.

Yong, A. C., Lam, N. T., and Menegon, S. J.: Closed-form expressions for improved impact resistant design of reinforced concrete beams, Structures, 29, 1828-1836, https://doi.org/10.1016/j.istruc.2020.12.041, 2021.

Yong, A. C., Lam, N. T., Menegon, S. J., and Gad, E. F.: Experimental and analytical assessment of flexural behavior of cantilevered RC walls subjected to impact actions, Journal of Structural Engineering, 146, 04020034, https://doi.org/10.1061/(ASCE)ST.1943-541X.0002578, 2020.

Yu, Z., Luo, L., Liu, C., Guo, L., Qi, X., and Zhao, L.: Dynamic response of flexible rockfall barriers with different block shapes, Landslides, 18, 2621-2637, https://doi.org/10.1007/s10346-021-01658-w, 2021.

Zhao, P., Xie, L., Li, L., Liu, Q., and Yuan, S.: Large-scale rockfall impact experiments on a RC rock-shed with a newly proposed cushion layer composed of sand and EPE, Engineering Structures, 175, 386-398, https://doi.org/10.1016/j.engstruct.2018.08.046, 2018.

Zhong, H., Lyu, L., Yu, Z., and Liu, C.: Study on mechanical behavior of rockfall impacts on a shed slab based on experiment and SPH–FEM coupled method, Structures, 33, 1283-1298, https://doi.org/10.1016/j.istruc.2021.05.021, 2021.

Zhong, H., Yu, Z., Zhang, C., Lyu, L., and Zhao, L.: Dynamic mechanical responses of reinforced concrete pier to debris avalanche impact based on the DEM-FEM coupled method, International Journal of Impact Engineering, 167, 104282-104301, https://doi.org/10.1016/j.ijimpeng.2022.104282, 2022.